POLITECNICO DI TORINO
Repository ISTITUZIONALE

Soil Displacement Estimation from Integrated Sensing Technologies in Data-Driven Models Biased by Temporal Coherence of PS-InSAR

Original
Soil Displacement Estimation from Integrated Sensing Technologies in Data-Driven Models Biased by Temporal Coherence of PS-InSAR / Tarantini, R., Miraglia, G., Coccimiglio, S., Ceravolo, R., Ferro, G.A.. - In: LAND. - ISSN 2073-445X. - 15:2(2026), pp. 1-24. [10.3390/land15020296]

Availability:
This version is available at: 11583/3007537 since: 2026-02-11T18:37:53Z

Publisher:
MDPI

Published
DOI:10.3390/land15020296

Terms of use:

This article is made available under terms and conditions as specified in the corresponding bibliographic description in the repository

Publisher copyright

(Article begins on next page)

30 October 2026

land

MDPI

Article

Soil Displacement Estimation from Integrated Sensing Technologies in Data-Driven Models Biased by Temporal Coherence of PS-InSAR

Raffaele Tarantini [1], Gaetano Miraglia [1,2,*], Stefania Coccimiglio [1], Rosario Ceravolo [1,2] and Giuseppe Andrea Ferro [1]

[1] Department of Structural, Geotechnical and Building Engineering, DISEG, Politecnico di Torino, 10129 Torino, Italy; raffaele.tarantini@polito.it (R.T.); stefania.coccimiglio@polito.it (S.C.); rosario.ceravolo@polito.it (R.C.); giuseppe.ferro@polito.it (G.A.F.)
[2] Responsible Risk Resilience Interdepartmental Centre (R3C), Politecnico di Torino, 10128 Torino, Italy
* Correspondence: gaetano.miraglia@polito.it; Tel.: +39-011-090-4884

Abstract

Spaceborne Synthetic Aperture Radar (SAR) interferometry provides long-term displacement measurements, but the quality of Persistent Scatterer (PS) time series depends critically on temporal coherence. Low-coherence points often exhibit auto-uncorrelated behaviours, which may be relevant to discriminate fast phenomena. This work introduces a coherence-based framework that identifies the coherence threshold beyond which PS displacement series retain sufficient reliability to support modelling. The threshold is estimated by analysing how data uncertainty, inferred through Sparse Bayesian Learning (SBL) techniques, varies with coherence and by detecting abrupt changes in this relationship. Once the optimal threshold is established, only the most reliable PS are used to train an SBL regression model linking satellite line-of-sight displacement to soil temperature and surface humidity measured by a low-cost ground sensor. PS-Interferometric SAR (PS-InSAR) time series are derived from COSMO-SkyMed raw images. The SBL model employs compressive-sensing principles and latent-parameter dictionaries of basis functions, whose latent parameters are calibrated through a constrained multi-start optimisation of a normalised residual-based objective function, regularised by a sub-validation dataset. In this work, it is shown that the trained model enables temporally denser reconstruction of displacement histories than the satellite revisit cycle allows and enables continuous soil monitoring by comparing model predictions with newly acquired PS-InSAR data.

Keywords: artificial intelligence; data integration; ground deformation; monitoring; MT-InSAR; PS-InSAR; sparse Bayesian learning; synthetic aperture radar

Check for updates

Academic Editors: Ebrahim Ghaderpour and Paolo Mazzanti

Received: 2 January 2026
Revised: 5 February 2026
Accepted: 6 February 2026
Published: 10 February 2026

Copyright: © 2026 by the authors. Licensee MDPI, Basel, Switzerland. This article is an open access article distributed under the terms and conditions of the Creative Commons Attribution (CC BY) license.

1. Introduction

Ground deformation monitoring is essential for managing geohazards and infrastructure risk, as land-surface movements may be driven by tectonic loading, slow landslides, consolidation of soft soils, groundwater drawdown, underground excavations and anthropogenic loading. Remote sensing, and in particular spaceborne SAR interferometry, has dramatically expanded the spatial and temporal coverage of deformation measurements, providing dense observations that complement sparse in situ networks. PS-InSAR identifies phase-stable radar targets and reconstructs their displacement histories from long

 https://doi.org/10.3390/land15020296

image stacks, overcoming many of the decorrelation limitations of conventional Differential InSAR (DInSAR) [1–3]. Multi-temporal InSAR contributions address mining-related subsidence and tailings-dam stability [4,5], landslide monitoring and forecasting, as well as slow-moving landslides and trend-turning-point detection [6,7], regional subsidence and hydro-geological processes [7], and ground deformation monitoring in volcanic island settings [8], highlighting issues related to time-series processing, multi-sensor integration and pre-processing-induced biases. Parallel developments in Structural Health Monitoring (SHM) have explored the integration of remote sensing and on-site measurements for monumental and infrastructural assets. For the Sanctuary of Vicoforte and other historic structures, long-term static and dynamic monitoring has been combined with Finite Element (FE) models to investigate the influence of soil-structure interaction and environmental conditions on modal parameters [9–11]. In particular, spaceborn Land Surface Temperature (LST) and Soil Water Index (SWI) have been exploited to interpret frequency fluctuations in terms of soil stiffness and saturation variations, suggesting a powerful role for geophysical satellite products in SHM protocols [11,12]. Despite this progress, soil displacement estimation from environmental data remains challenging. Subsurface conditions are only partially constrained by standard geotechnical investigations, soil behaviour is non-linear and history-dependent, and the inversion problem is often ill-posed. Bayesian approaches and surrogate modelling have, therefore, been increasingly adopted to infer soil parameters and their uncertainty from combinations of monitoring data and numerical simulations. Within this context, the quality and representativeness of satellite-derived time series to the inversion are critical. Among the various remote sensing approaches for monitoring ground deformation, PS-InSAR has emerged as a particularly powerful technique, especially in urban and built environments [13–17]. By identifying radar targets that remain phase-stable over long time periods, PS-InSAR allows for millimetric-level displacement measurements and good reconstruction of long-term deformation trends. Its strength lies in the ability to provide reliable time series even in the presence of atmospheric noise and temporal decorrelation, making it well-suited for monitoring soil, infrastructure, buildings, and heritage structures. Although PS-InSAR has proven effective for measuring structural displacements, existing methods have significant limitations. Spatial coverage is often limited, and soil deformation estimates may be biased due to sampling issues. Furthermore, systematic integration with in situ measurements and explicit uncertainty quantification remain underexplored. The influence of temporal coherence on PS selection and its impact on sampling bias will be formally addressed in the proposed methodology. In this manuscript, PS-InSAR is employed to investigate ground settlements, with specific attention given to the formalisation of temporal coherence and its impact on the definition of deformation time series. The PS-InSAR is used in order to introduce a coherence-based framework that identifies the coherence threshold beyond which PS displacement series retain sufficient reliability to support modelling. The selected PS-InSAR data are then integrated with in situ monitoring measurements to support the prediction of displacement time series useful for assessing the structural health of the soil under investigation. The proposed approach follows some key steps: PS-InSAR points are selected based on temporal coherence to ensure reliable measurements, and Line of Sight (LOS) displacement time series are extracted. These are combined with in situ surface soil temperature and humidity data and used as inputs to an SBL surrogate model, which reconstructs soil settlements and estimates their uncertainty. Temporal coherence is treated as a design variable: by analysing its relationship with predictive uncertainty, the minimum coherence threshold for reliable monitoring is defined. In this way, the method integrates remote sensing and in situ data to track both slow settlements and dynamic soil behaviour. Further details on the methodology can be found in the dedicated section and in the corresponding Figure 1. The

approach demonstrates that low-cost in situ sensors can effectively complement remote sensing for continuous monitoring of soil behaviour.

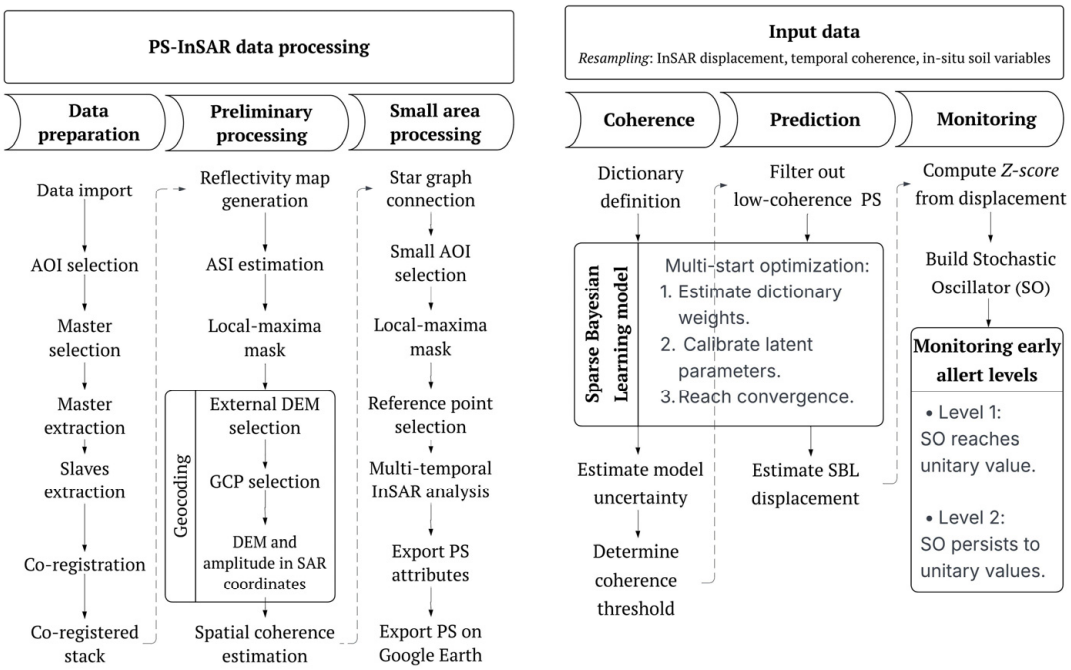


Figure 1. Flow-chart of the methodology: PS-InSAR data processing (**a**); SBL methodology (**b**). Solid arrows indicate the sequence of tasks within each macro-process, while dashed arrows indicate transitions between the two macro-processes.

The objective of this paper is to: (i) formalise the role of temporal coherence in PS-InSAR processing and clarify how it affects the deformation time series prediction; (ii) develop a coherence-aware framework in which LOS displacements of PS located on a sufficiently stiff structural basement are used as proxies for ground deformations, and are integrated with in situ monitoring through a surrogate model trained via SBL; and (iii) provide a conceptual and methodological study of how coherence thresholds and weighting strategies influence the posterior distribution of surrogate model parameters used in predict soil displacements. In the application, only PS belonging to the lowest part of the basement are selected, and their displacements are interpreted as representative of the soil settlements at the base of the structure.

The manuscript is organised as follows. Section 2 presents an overview of the background of InSAR data processing. Section 3 outlines the methodology adopted in this study. Sections 4 and 5 describe, respectively, the case study in which the proposed methodology is applied and the corresponding results. Finally, Section 6 summarises the main conclusions of the study.

2. Background of InSAR Data Processing

2.1. Multi-Temporal Time Series InSAR and PS-InSAR

Repeat-pass InSAR measures phase differences between complex SAR images, acquired from nearly the same viewing geometry at different times, to estimate changes in range distance between the sensor and the ground. For interferogram i and persistent

scatterer p, the wrapped interferometric phase can be written as the superposition of several contributions,

$$\phi_i(p) = \phi_i^{topo}(p) + \phi_i^{def}(p) + \phi_{\mathrm{i}}^{\mathrm{atm}}(\mathrm{p}) + \phi_{\mathrm{i}}^{\mathrm{orb}}(\mathrm{p}) + \phi_{\mathrm{i}}^{\mathrm{noise}}(\mathrm{p}) \quad (1)$$

where $\phi_i^{topo}(p)$ is the residual topographic term, mainly due to inaccuracies in the reference Digital Elevation Model (DEM) and/or residual height errors of the scatterer (its magnitude is strongly controlled by the perpendicular baseline); $\phi_i^{def}(p)$ the deformation contribution, proportional to the LOS range change, induced by true motion of the target (a 2π phase cycle corresponds to a LOS displacement of $\lambda/2$, with λ the radar wavelength); $\phi_{\mathrm{i}}^{\mathrm{atm}}(\mathrm{p})$ accounts for atmospheric path delay variations; $\phi_{\mathrm{i}}^{\mathrm{orb}}(\mathrm{p})$ represents the residual orbital term, often appearing as long-wavelength phase ramps; and $\phi_{\mathrm{i}}^{\mathrm{noise}}(\mathrm{p})$ groups phase noise sources, such as thermal noise and decorrelation effects (temporal and geometric decorrelation, unmodelled scattering changes) [1,3,18]. Multi-temporal InSAR techniques exploit long image stacks to separate these contributions and to retrieve displacement time series at each resolution cell.

PS Interferometry (PSI) was originally developed at Politecnico di Milano and has become a standard for millimetre-scale monitoring of surface deformation in urban and infrastructural settings [1,18]. PSI identifies phase-stable "permanent scatterers" whose complex backscatter remains coherent over time. For each PS, the differential phase is modelled as a function of unknown deformation, residual height and atmospheric terms, and a network of interferograms is solved via linear or non-linear regression. Stanford Method for PS (StaMPS) and related approaches extend PS techniques to non-urban and low-coherence terrains by robustly identifying pixels with low phase variance [2]. Small Baseline Subset (SBAS) methods adopt a complementary strategy based on interferograms with limited temporal and perpendicular baselines, forming subsets that are later recombined into deformation time series [19]. While SBAS generally provides better performance over spatially correlated but moderately coherent surfaces, PS-InSAR offers superior precision and temporal continuity for discrete, highly coherent points. PSI has been comprehensively reviewed by Crosetto et al. (2016) [3], who emphasise its suitability for monitoring urban areas, infrastructure and slow deformation processes, including subsidence, landslides and structural movements. In this work, the authors adopt a PS-InSAR approach consistent with the POLIMI PS/QPS formulation [20,21], which is also implemented in SARPROZ and other MT-InSAR tools. For each PS p and differential interferogram i, characterised by a normal baseline B_i^n and temporal baseline B_i^t with respect to a common master acquisition, the wrapped differential phase relative to a reference PS p_0 is written as

$$\phi_i(p) = \phi_i^H(p) + \phi_i^D(p) + \phi_i^{APS}(p) + \phi_i^{noise}(p) \quad (2)$$

where $\phi_i^H(p)$ is the residual topographic phase due to DEM errors, $\phi_i^D(p)$ is the deformation-related phase, $\phi_i^{APS}(p)$ represents the Atmospheric Phase Screen (APS) and $\phi_i^{noise}(p)$ collects decorrelation and other unmodelled contributions. Equation (2) highlights that PSI is solved in a differential form with respect to a reference PS: common-mode contributions (e.g., orbital ramps and part of the APS) are reduced, and the remaining terms are estimated through the interferogram network. Under the standard small-deformation, long-wavelength approximation, the height and mean LOS velocity contributions for a target at residual height Δh_p and LOS velocity Δv_p both relative to p_0 are modelled, following the PS formulation adopted in SARPROZ [22,23], as

$$\phi_i^H(p) = \frac{4\pi}{\lambda} \frac{\Delta h_p}{R_0 \sin\theta} B_i^n \quad (3)$$

$$\phi_i^D(p) = \frac{4\pi}{\lambda}\Delta v_p B_i^t \tag{4}$$

where λ is the radar wavelength, θ is the local incidence angle, and R_0 is the slant range to the reference target. In SARPROZ, this linear model can be extended by enriching $\phi_i^D(p)$ with deterministic components that account, for instance, for seasonal and temperature-dependent terms, but the core inversion for Δh_p and Δv_p remains governed by the expressions above. Equations (3) and (4) provide the sensitivity of phase to (i) residual height errors through the perpendicular baseline term, and (ii) mean LOS velocity through the temporal baseline term; these two contributions form the core linear model inverted in PS processing before adding optional deterministic components (e.g., seasonal/thermal terms). Candidate PSs are identified as local amplitude maxima satisfying user-defined criteria on amplitude stability and multi-look intensity, following the strategy adopted for high-accuracy PS-based DEM reconstruction. In the present work, such criteria are implemented via the SARPROZ local-maxima mask and an amplitude-thresholding procedure, ensuring that only scatterers with sufficiently stable backscatter are retained for subsequent time-series analysis. All PS-InSAR processing is performed in small-area mode, which is particularly suited to structural-scale applications and allows the joint estimation, for each selected PS, of residual height, linear and seasonal deformation components, and a set of quality indicators, including temporal coherence and phase-residual standard deviation, (in the software these indicators are called respectively COHER and STDEV), as exported by the SARPROZ sparse-data modules. The specific processing choices (orbit selection, interferogram network, reference point, coherence thresholds and small-area definition) adopted in the application to the soil of the Vicoforte sanctuary are described in detail in the Application Section of the paper.

2.2. Temporal Coherence in PS-InSAR

Temporal coherence is a complex-valued, normalised measure of the stability of the interferometric phase over time. After removing the contributions of the assumed deformation model, residual topography and other deterministic terms, the residual phases of a pixel are used to estimate its coherence, typically as the magnitude of the average complex exponential of residual phases. For each PS p, following the implementation adopted in SARPROZ and related PS/QPS codes, a complex temporal coherence ξ_p is first computed as

$$\xi_p = \frac{1}{M}\sum_{i=1}^{M} exp(jr_i(p)) \tag{5}$$

where $r_i(p)$ are the residual phases for the M interferograms associated with that PS, and j is the imaginary unit. The temporal coherence γ_p is then defined as the modulus of ξ_p:

$$\gamma_p = |\xi_p| \tag{6}$$

γ_p can vary within a range from 0 to 1: values close to one correspond to highly stable scatterers, whereas values near zero indicate strong decorrelation. Temporal coherence is influenced by land cover and scatterer type, soil conditions and moisture, acquisition geometry and temporal sampling, as well as processing decisions. Buildings, rock outcrops and other rigid surfaces tend to maintain high coherence; vegetation, ploughed fields and water bodies decorrelate rapidly. Changes in soil moisture modify dielectric properties and scattering mechanisms, especially at C- and X-band, reducing coherence over soils. Long temporal baselines, large perpendicular baselines and significant incidence-angle variations generally reduce coherence. Finally, interferogram network design, filtering, phase unwrapping, DEM correction, and the chosen deformation model all affect residual

phases and the resulting coherence estimates. In practice, temporal coherence is used as a selection criterion, where a minimum coherence or amplitude-dispersion threshold defines the PS set. However, coherence is not a pure noise metric: it is correlated with the physical nature of the scatterer and with the deformation process itself. Coherence-based selection, therefore, generates a biased sampling of the deformation field that typically favours man-made structures and neglects softer soils and vegetated areas. For soil displacement estimation, this has two major consequences. First, the PS-InSAR time series used for calibration are spatially and physically biased towards highly coherent scatterers. Second, decisions on coherence thresholds directly affect the posterior of soil displacements obtained from data-driven models. In the framework proposed here, coherence is, therefore, treated not only as a quality indicator, but as an explicit design variable: PS displacement histories, together with their temporal coherence, are propagated into the likelihood function of the surrogate-based soil displacement model, ensuring a coherence-aware treatment of model uncertainty and providing a basis for defining application-specific "optimal" coherence thresholds.

3. Methodology

3.1. Coherence-Based Soil Monitoring Concept

The proposed framework views the soil as an evolving system in time under environmental and hydro-geological forcing. The practical difficulty is that continuous in situ monitoring of the soil is rarely feasible at heritage sites, whereas high-coherence PS-InSAR measurements are typically concentrated on structural elements rather than on soft ground. The authors, therefore, adopt a coherence-aware strategy in which basement PS-InSAR displacements, soil temperature and soil surface moisture measurements are combined through an SBL surrogate to infer soil displacement time-histories and their evolution. A central modelling assumption is that the structural basement behaves as a sufficiently rigid raft. Previous dynamic studies on the soil of the Sanctuary of Vicoforte have shown that the dominant structural modes lie in a relatively low-frequency band (e.g., 1–7 Hz), while simplified 1D site-response analyses and in situ tests indicate soil fundamental frequencies at higher values (e.g., 9–16 Hz) [24–28].

Within the rigid-basement assumption, PS-InSAR processing is restricted to PS located on the base of the basement. Their LOS displacement time series are interpreted as measurements of the motion at the soil, including both quasi-static settlements and low-amplitude dynamic components. PS is obtained in small-area PS mode using COSMO-SkyMed data and the SARPROZ implementation of the POLIMI model, which jointly estimates residual height, deformation parameters and temporal coherence for each candidate scatterer. Temporal coherence and residual phase dispersion are then used to define families of PS sets: high-coherence PS provide more reliable but spatially sparse constraints, while including lower-coherence PS increases spatial sampling at the cost of larger phase noise and potential bias. The link between these observables and soil in situ measures is provided by a data-driven SBL model of the soil. Rather than constructing a complex and often uncontrollable FE model, a surrogate is constructed using SBL [29,30]. In its most general form, the surrogate maps soil in situ measures to a set of features extracted from the PS-InSAR LOS time series (e.g., secular and seasonal components) and affected by noise [31].

3.2. PS-InSAR Data Processing

The processing follows the same small-area PS/QPS strategy previously introduced.

A stack of calibrated COSMO-SkyMed SLC images is first co-registered to a common master, and images are connected according to a star-shaped graph centred on the master

for the subsequent PS solution. Candidate scatterers are identified using reflectivity and amplitude-stability diagnostics: a local-maxima mask is applied to the mean-amplitude image, and pixels with sufficiently stable amplitude are retained as potential PS. An external DEM (e.g., Copernicus) and one or more ground control points are used to remove the bulk topographic phase and to anchor the solution in a geodetic reference frame. Temporal coherence is estimated in a multi-image InSAR stage on the full stack before restricting the analysis to the area around a structure. Images are first organised in a Minimum-Spanning-Tree (MST) or similar low-redundancy graph to minimise decorrelation and to optimise phase unwrapping. For each candidate PS, a preliminary height–velocity model is fitted and removed, and the residual phases are used to compute the complex temporal coherence as the average of unit phasors over the interferogram network; its modulus defines the temporal coherence, while the residual phase dispersion provides a complementary noise measure. These quantities are exported as standard PS attributes (e.g., COHER) and later used both to select high-quality PS within a small area centred on the structural. The small-area processing step then solves, for the selected basement PS, a parametric model, including residual height, linear deformation rate and, when needed, thermal or seasonal terms, yielding geocoded LOS displacement time series that form the InSAR input to the subsequent soil analysis.

3.3. Sparse Bayesian Learning and Coherence-Based Modelling

The relationship between environmental variables measured in situ and the displacements observed through PS-InSAR is modelled using an SBL approach, formulated as a probabilistic regression problem, denoted as follows:

$$\boldsymbol{x}(t) = \left[x_1(t), x_2(t)\right]^T \tag{7}$$

As the input vector (temperature and surface soil moisture) and $y(t)$ as the displacement along the satellite line of sight, the model takes the form:

$$y(t) = \Gamma\left(\boldsymbol{x}(t)\right)^T \boldsymbol{w} + \varepsilon(t) \tag{8}$$

where $\Gamma(\cdot)$ is a dictionary of nonlinear basis functions, and $\varepsilon(t)$ represents a zero-mean Gaussian noise term with variance σ^2. In the Bayesian framework, the weights $\boldsymbol{w}$ are associated with a zero-mean Gaussian prior distribution with diagonal covariance matrix $\mathbf{A}$:

$$p(\boldsymbol{w} \mid \boldsymbol{\alpha}) = N\left(\mathbf{0}, \boldsymbol{A}^{-1}\right) \tag{9}$$

where $\boldsymbol{A} = \mathrm{diag}(\alpha_1, \ldots, \alpha_K) \in K \times K$ and each hyperparameter α_k controls the relevance of the corresponding basis function. During the learning phase, many α_k tend to large values, forcing the associated weights toward zero and producing a sparse representation of the output. Conditioned on the optimal hyperparameters, the posterior distribution of the weights is as follows:

$$p(\boldsymbol{w} \mid y) = N(\boldsymbol{\mu}_w, \boldsymbol{\Sigma}_w) \tag{10}$$

with

$$\boldsymbol{\Sigma}_w = \left(\boldsymbol{A} + \sigma^{-2}\boldsymbol{\Gamma}^{*T}\boldsymbol{\Gamma}^{*}\right)^{-1} \textit{ and } \boldsymbol{\mu}_w = \sigma^{-2}\boldsymbol{\Sigma}_w\boldsymbol{\Gamma}^{*T}y \tag{11}$$

where $\boldsymbol{\Gamma}^{*} \in N \times K$ is the design matrix built by evaluating the basis functions on the observed inputs N. For a new observation $\boldsymbol{x}^{*}$, the prediction is described by a Gaussian predictive distribution:

$$p(y^{*} \mid \boldsymbol{x}^{*}, y) = N\left(\mu_{*}, \sigma_{*}^2\right) \tag{12}$$

with

$$\mu_* = \Gamma\left(\boldsymbol{x}^*\right)^T \boldsymbol{\mu}_w \text{ and } \sigma_*^2 = \sigma^2 + \Gamma\left(\boldsymbol{x}^*\right)^T \boldsymbol{\Sigma}_w \Gamma(\boldsymbol{x}^*) \quad (13)$$

The term σ_*^2 provides an explicit estimate of the predictive uncertainty associated with each time point. In the proposed framework, the temporal coherence of PS-InSAR enters the model indirectly. PS characterised by different levels of coherence produces time series with varying levels of residual noise, which directly affect the predictive variance estimated by SBL. By analysing the dependence of the temporal mean uncertainty $\overline{\sigma}_*$ on coherence γ_p, it is possible to identify a transition between a low-reliability (high variance) and a stable behaviour. Coherence is, therefore, treated not as an a priori threshold, but as a design variable in the optimisation of the predictive model. The optimal threshold γ_{th} is identified from the point where predictive uncertainty shows a sudden increase. In this way, the uncertainty estimate provided by SBL becomes the quantitative tool for defining the minimum coherence level required for PS-InSAR time series to be informative and usable for reliable monitoring of soil conditions over time.

Within the methodology, the dictionary of basis functions is defined as the combination of two main families of functions. The first family aims at capturing periodic behaviours in the data and is modelled through a Fourier series. The second family is designed to describe non-oscillatory trends and long-term behaviours, which are represented using polynomial series. For both families, the unknown parameters include the order of the series, which is not imposed a priori but can be estimated through any inverse modelling procedure. In this work, the authors adopted a multi-start, gradient-based optimisation strategy. The procedure consists of solving the inverse problem multiple times, starting from different initial conditions, reducing the risk of convergence towards local minima. For each initialisation, a gradient-based optimiser is employed to minimise the objective function associated with the model residuals, while simultaneously promoting sparsity within the selected set of basis functions. The solution providing the best trade-off between data fitting accuracy and model complexity is then retained as the optimal representation. Figure 1 reports the flow-chart of the framework proposed in the paper.

4. Application

4.1. Site Layout

The stratigraphic configuration of the Vicoforte soil area, as reconstructed based on the geognostic and geotechnical investigations reported in [32], reveals a succession of soils consistent with the hilly context of the Monregalese sector, characterised by fine-grained cover deposits resting on older formations with predominantly cohesive behaviour. The typical stratigraphy, defined through continuous core drilling and in situ tests, shows a lateral homogeneity, with limited variations in thickness. The first superficial horizon consists of a layer of fill material and topsoil, generally less than 1.0–1.5 m thick. This layer exhibits poor mechanical properties, high compressibility, and low shear strength, making it unsuitable for supporting structural loads. Beneath it lies a level of clayey silts and silty clays of grey-brown colour, locally with fine sandy intercalations. These soils display a consistency ranging from medium to stiff, with a medium plasticity index and water content close to or slightly above the plastic limit. From a mechanical point of view, these layers present moderate undrained cohesion values and low effective friction angles, indicative of predominantly cohesive behaviour. Laboratory tests highlight medium-to-high compressibility, with oedometer moduli compatible with weakly to normally consolidated fine soils. The permeability is low, influencing the dissipation times of excess pore pressures in the event of rapidly applied loads. At greater depths, more compact layers are encountered, attributable to marls and marly clays, sometimes weakly cemented.

These horizons represent the geotechnical reference substrate and exhibit better mechanical characteristics, with a significant increase in shear strength and reduced deformability. Drained strength parameters indicate modest effective cohesion values but higher friction angles compared to the overlying layers, suggesting greater overall stability. Figure 2 reports a map view of the site, with the analysed soil area in the bottom left part.



Figure 2. Map view of the site by Google Maps.

In consideration of the geotechnical characteristics and the importance of the site, the soil close to the Sanctuary of Vicoforte is subject to a continuous monitoring system. Specifically, three piezometers are installed to monitor the trend of water table level, along with a thermo-hygrometer to measure surface soil humidity and temperature. All sensors are located in the south-western sector of the Sanctuary, where the clayey silt layer is thicker and more sensitive to hydro-mechanical variations. Figure 3 reports the location of the soil in situ monitoring system. In the figure, PZ01, PZ02, and PZ03 stand for piezometers, while TERMOIGROT_1 defines the position of the thermo-hygrometer used in the study.

The in situ sensor deployed within the study area is not intended to provide a point-wise physical representation of local soil behaviour. Rather, it is used as a variable that exhibits a strong correlation with the satellite-derived displacement measurements. In particular, the local effects of temperature and humidity, especially temperature, can be associated with a spatially broader area than the specific monitoring point. Under quasi-stationary conditions, the soil surface temperature tends to equilibrate with air temperature, which generally exhibits limited spatial variability, except for highly localised temporary effects (e.g., shadow). As a consequence, within a small range of variability, the correlation between temperature and displacement remains valid over spatially distributed zones. It is acknowledged that the present study also employs a single in situ sensor as a demonstrative example of the proposed methodology. Nevertheless, the availability of additional sensors would further improve the robustness of the approach, as the corresponding data would enrich the dictionary of basis functions adopted within the Sparse Bayesian Learning framework.

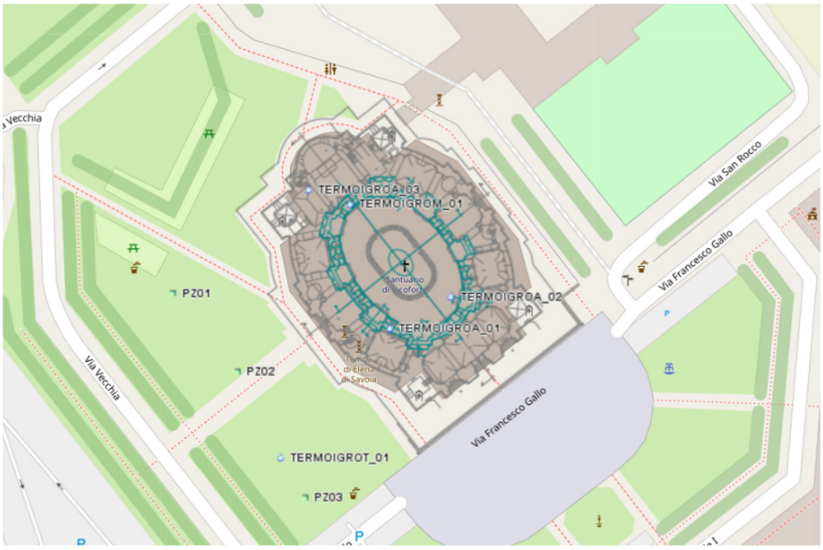


Figure 3. Location of the soil monitoring system (where TERMOIGRO "A", "M" and "T" indicates the location of thermo-hygrometers for air, masonry and soil, and PZ the location of piezometers, the other terms in the figures define the names of the streets).

4.2. Experimental Data

This section describes the set of experimental data used in the study, with particular reference to the available sensors and the criteria adopted for selecting the measurements employed in the analyses. The experimental data are divided into two main categories: data acquired through sensors installed in situ and data from remote sensors belonging to a satellite constellation. The in situ sensors include instruments for monitoring the hydrological and thermo-hygrometric conditions of the soil. Specifically, measurements of the groundwater table height, surface soil temperature, and surface soil moisture are available. The groundwater table height is measured through piezometers installed in the subsoil, while the surface soil temperature and moisture are acquired using a soil thermo-hygrometer. Since one of the main objectives of the work is the reproduction of satellite displacement data using low-cost sensors, it was decided not to use, in the subsequent analyses, the data provided by the piezometers. Although these instruments guarantee a direct and reliable measurement of the groundwater level, they involve high installation and management costs, making their adoption in widespread monitoring systems unsustainable.

This choice is further justified by the fact that the temporal trend of the groundwater level closely follows that of surface soil moisture, as shown in Figure 4. Consequently, to describe the surface hydrological conditions and their role in deformation processes, only soil moisture and temperature data acquired through the thermo-hygrometer were used. Figure 5 shows the temporal trend of these quantities, measured with a sampling time of 1 h, highlighting variations consistent with seasonal cycles and significant meteorological events. In more detail, it is possible to see how the maximum temperature points reached in the summer season correspond to lower humidity values.

As for the remote sensing data, they come from the COSMO-SkyMed satellite constellation and provide information on ground surface and structure displacements along the sensor LoS, at points characterised by high radar reflectivity. Unlike in situ data, for the satellite displacement data, the analysis was carried out directly on raw scenes, without referring to pre-processed products. This choice allowed a greater control over the entire ensuring a customised integration with ground experimental data. Figure 6 shows the final result obtained after processing the satellite scenes, highlighting the temporal evolution of the measured displacements. In the figure, it is possible to note that a lot of points

present a linear trend, with maximum reached displacements of approximately 400 mm. The LoS InSAR data processing procedures are described in detail in the following section, specifically dedicated to the processing of satellite displacement data.

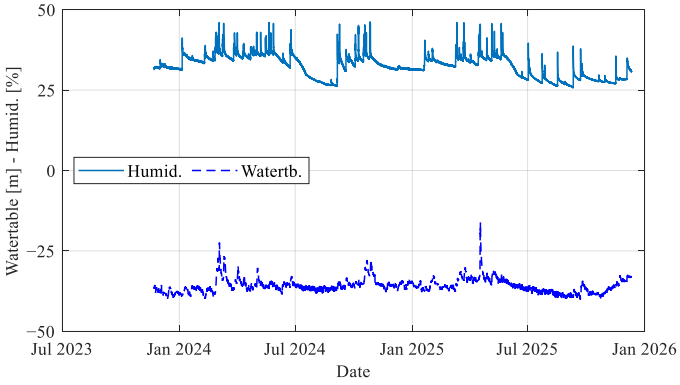


Figure 4. Comparison of the time behaviour of water table level and surface soil moisture.

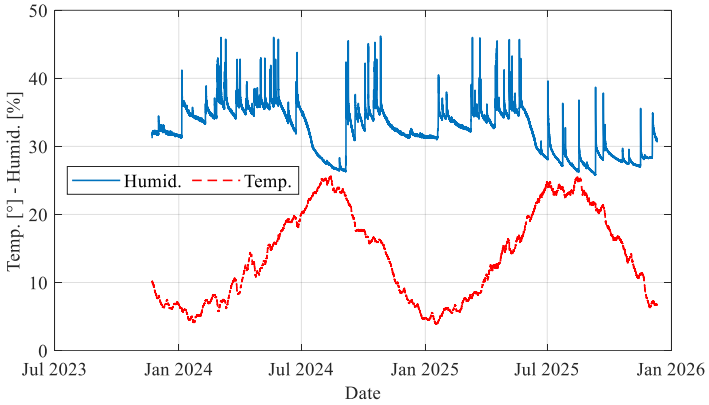


Figure 5. Surface soil moisture and surface temperature data used in the study.

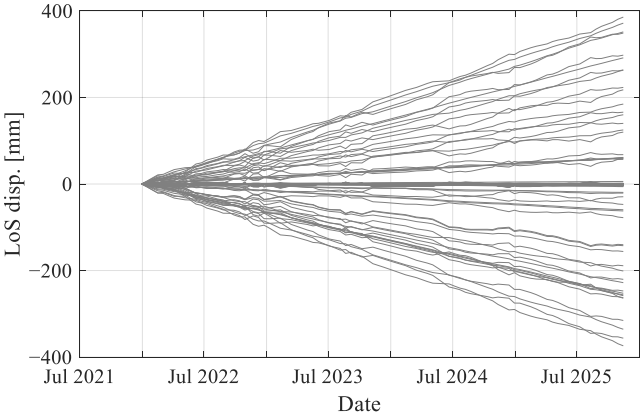


Figure 6. LoS InSAR displacements obtained for the studied site.

4.3. In Situ Data Processing

This section describes the processing procedures applied to the data acquired in situ, with the aim of making them consistent and directly comparable with the displacement measurements derived from satellite remote sensing. The data processing was aimed at building a synchronous dataset suitable for subsequent correlation analysis and predictive modelling of surface displacements observed through the InSAR technique. A preliminary analysis was conducted using graphical representations of the time series. The joint analysis of soil temperature and moisture allowed the evaluation of their seasonal and short-term

variability, while the visualisation of LoS time series provided an initial indication of the amplitude and dispersion of the displacements measured by the satellite sensors, including their trend. Subsequently, the processing concerned the temporal resampling of the in situ data. Since the objective of the work is to reproduce the satellite displacement signal using only data from low-cost sensors, it was necessary to adopt a unique temporal resolution. Specifically, the soil temperature and moisture data were resampled to the largest sampling interval, coinciding with that of the satellite interferometric observations, approximately 15 days. The resampling was carried out through temporal interpolation, using the acquisition dates of the satellite scenes as a reference and limiting the analysis to the time windows common to both monitoring systems, remote and local. Figure 7 shows the time series of surface soil moisture and temperature resampled on the temporal support of the satellite data. Although these series are under-sampled compared to the original hourly signal, they retain the main informational content associated with medium- and long-term variations, particularly seasonal and inter-seasonal ones. The loss of information mainly concerns the faster variations, such as daily ones, which are not directly observable at the temporal step of satellite acquisitions; however, the most important information of the inverse correlation between temperature and surface soil humidity is still maintained.

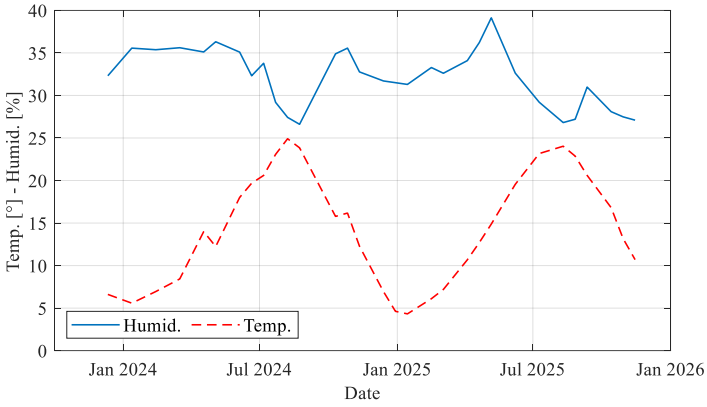


Figure 7. Time-history of surface soil moisture and surface temperature resampled to the time support of satellite data.

4.4. Hyperparameters and Variable Setting for Modelling

For modelling purposes, the overall time dataset was divided into three subsets in order to ensure proper model training and avoid overfitting phenomena. Specifically, the input variables consist of the interpolated time series of soil temperature and moisture, while the output variable is represented by the displacement along the line of sight measured by the satellite sensors. The dataset was divided into three parts: a training subset, a validation subset, and a testing subset. Thirty percent of the overall data was reserved for testing and was completely excluded from the model training phase. The remaining 70% of the dataset was equally split between training (35%) and validation (35%). The training subset was used for optimising the parameters of the SBL model, while the validation subset was employed to assess the model generalisation capability during the learning phase. In the SBL model, the optimised parameters include the weights associated with the selected basis functions, as well as two latent parameters that control the expansion order of a polynomial basis and a trigonometric basis. These expansions allow a more scalable representation of both slow nonlinear components and any periodicities present in the input time series. The learning algorithm also introduces a penalty term in the objective function, based on the difference between the training error and the validation error. This term helps limit model complexity and reduce the risk of overfitting. In the cost function minimised by the model, a weight of 50% was assigned to the error term

calculated on the training dataset and a weight of 50% to the penalty term, defined as the absolute difference between the training error and the validation error. The optimisation process was also limited to a maximum of 100 iterative cycles, and an early stopping criterion based on parameter convergence was introduced, according to which the algorithm terminates if the normalised difference between two estimates of the weights is less than 1×10^{-6}. Then, the implemented method to minimise the cost function adopted a global optimisation strategy based on multi-start initial points for the latent parameters, aimed at reducing dependence on the initial point and increasing the likelihood of identifying a global minimum. Starting from a main initial parameter vector, multiple perturbed initial configurations are generated by introducing variations proportional to the values of the parameters themselves. Each initial configuration is then subjected to a constrained local optimisation using a quasi-Newton method (trust-region algorithm based on gradient), which exploits derivative information to quickly converge toward a local minimum. The local solutions obtained from all initial points are compared, and the one that minimises the objective function is selected as the final solution.

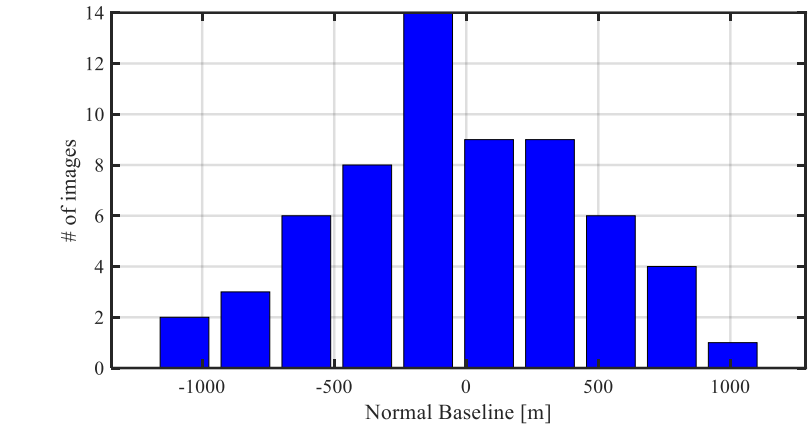
5. Results and Discussion

5.1. PS-InSAR Time Series

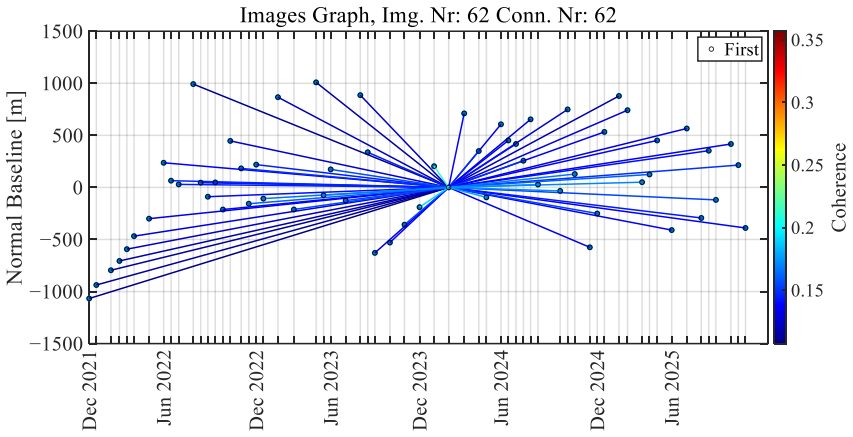
PS-InSAR processing for the area close to the Sanctuary of Vicoforte is performed in small-area PS/QPS mode, following the POLIMI formulation and its implementation in SARPROZ. The dataset consists of 62 COSMO-SkyMed (Second Generation) SLC images (stack identifier STR-005) acquired in HH polarisation between 29 December 2021 and 14 November 2025 over a scene of approximately 3 km $\times$ 3 km centred on the monument. Acquisitions were collected in StripMap mode, ascending, right-looking geometry, with a scene-centre incidence angle of 29.4° (angle from the local vertical at ground). The processed data have a ground pixel spacing of 2.18 m (range) $\times$ 2.25 m (azimuth). Operating at X-band (λ = 0.0312 m), the dataset provides an average effective revisit time of approximately 23.2 days over the site. All SLCs are co-registered to a common master dated 13 February 2024 (20240213_HH). The distribution of acquisitions with respect to normal baselines is summarised in Figure 8a, while Figure 8b illustrates the star-shaped interferometric graph used for the PS solution, with edges coloured according to the average spatial coherence. A Copernicus DEM is used to remove the bulk topographic phase, and the regional setting is shown in Figure 8c. A ground control point located on a reflective and stable point (44.361887° N, 7.862178° E) anchors the solution in a geodetic reference frame.

A local-maxima mask is applied to the mean-amplitude image. The reflectivity map, the position of the Ground Control Point (GCP) and the main clusters of candidate PS are shown in Figure 9a, while Figure 9b illustrates the Amplitude Stability Index (ASI) and spatial coherence over the full frame. Temporal coherence is then estimated on the full stack before restricting the analysis to the monument. For this purpose, images are connected through an MST graph to minimise spatial and temporal baselines and to facilitate phase unwrapping. For each candidate PS, a preliminary height–velocity model is fitted and removed; the residual phases over the MST network are used to compute the complex temporal coherence as the average of unit phasors, whose modulus defines the temporal coherence, while the residual phase dispersion provides a complementary noise measure. These quantities are exported as standard PS attributes (COHER and STDEV) and later serve both to select high-quality PS within a small area encircling the structural basement and to define coherence-dependent weights in the multi-image inversion. In the final small-area processing step, the analysis is restricted to the footprint of the Sanctuary and its immediate surroundings. PS is re-selected within this window using the local-maxima mask and the amplitude threshold, and a reference point is chosen at the base of the

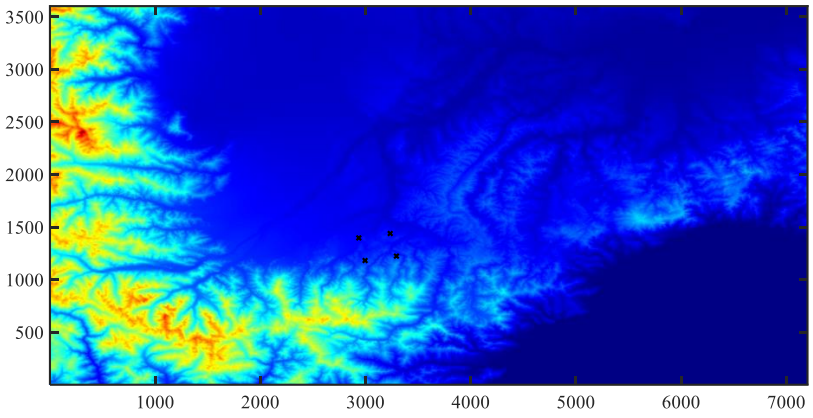
structure, with high amplitude and high temporal coherence, to minimise residual orbital and atmospheric artefacts. The reflectivity map regarding the small area is shown in Figure 10a. Figure 10b–d summarise, respectively, the temporal coherence, the mean LOS velocity and the cumulative LOS displacement of the small-area PS, together with their empirical distributions.



(**a**)



(**b**)



(**c**)

Figure 8. (**a**). Normal baseline histogram with respect to the selected master image (13 February 2024) (**b**). Star-shaped interferometric graph centred on the master acquisition, with edges coloured according to the average spatial coherence (**c**). Copernicus DEM, area of interest (AOI) within the black crosses.

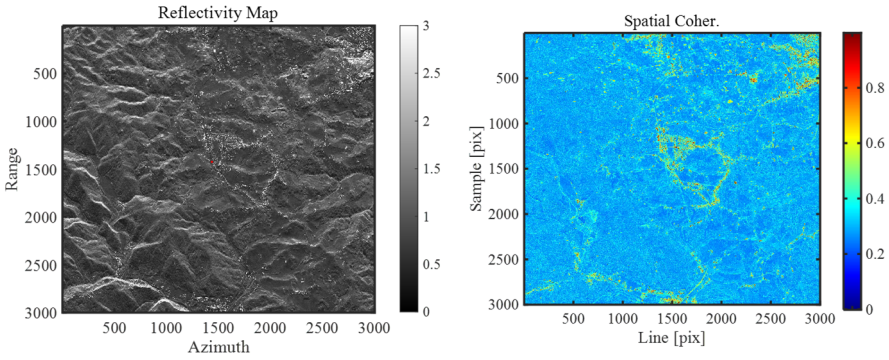


Figure 9. Mean reflectivity (amplitude) map of the COSMO-SkyMed stack over the Vicoforte area, showing the location of the ground control point in red (**a**). Spatial coherence (**b**).

For each selected basement PS, a parametric model is solved that includes residual height, linear LOS deformation rate and a thermoelastic component driven by air temperature, so that seasonal and temperature-dependent effects are explicitly represented in the time series. The resulting geocoded LOS displacement histories at the soil-structure interface constitute the PS-InSAR output to the surrogate model, which links these displacements, together with soil surface temperature and humidity. The spatial distribution of small-area PS on Google Earth 2D and 3D renderings is illustrated in Figure 11a,b. Figure 11c presents example amplitude and LOS displacement time series for a representative basement PS, illustrating the high temporal coherence and the seasonal thermoelastic component captured by the adopted parametric model.

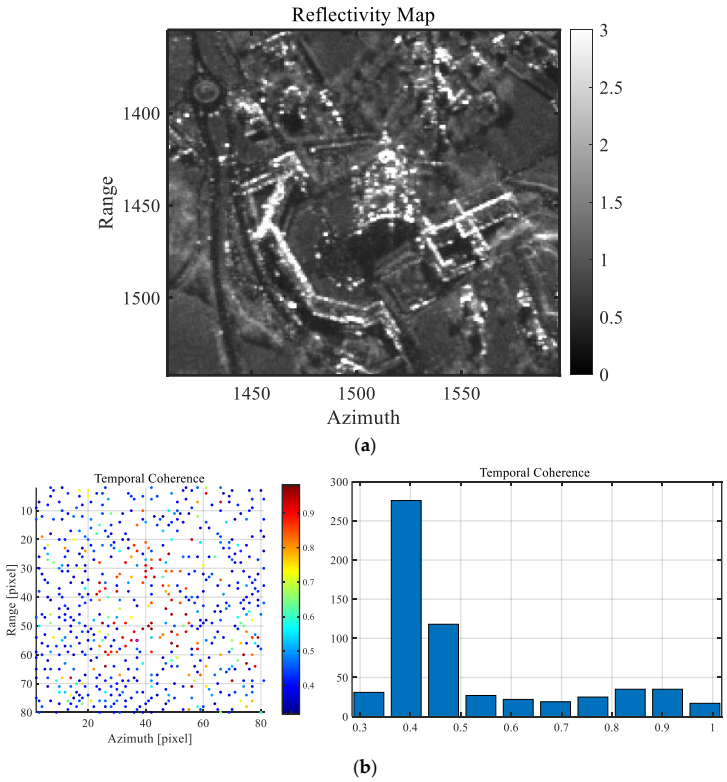


Figure 10. *Cont.*

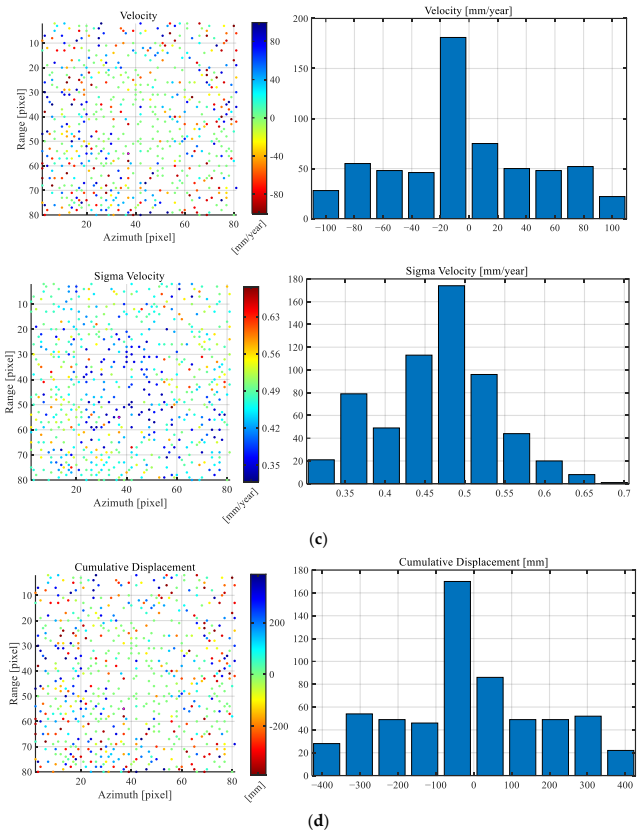


Figure 10. Small-area reflectivity map centred on the Sanctuary of Vicoforte (**a**), temporal coherence of the selected PS (**b**), mean LOS velocity of the selected PS (**c**), cumulative LOS displacement of the selected PS over the observation period (**d**).

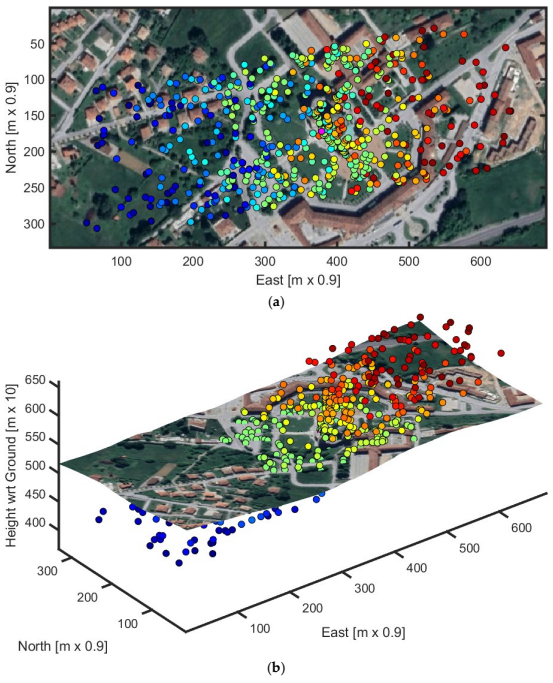
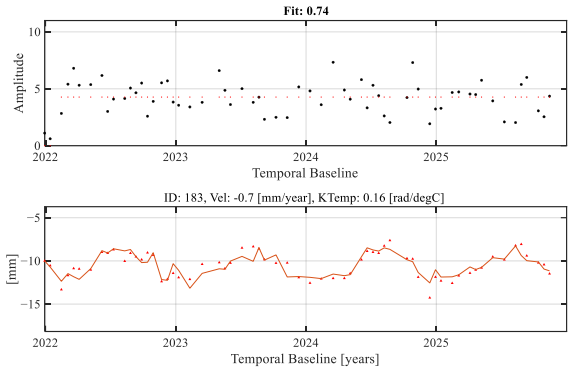


Figure 11. *Cont.*



(**c**)

Figure 11. Spatial distribution of small-area PS overlaid on a Google Earth 2D (**a**) and 3D (**b**) view of the Sanctuary of Vicoforte. Example amplitude and LOS displacement time series for a representative basement PS, showing the seasonal thermoelastic component (**c**). Black dots represent individual amplitude measurements, while red circles indicate the mean value. Red triangles represent individual LOS displacement values, and the solid red line interpolates the displacement trend.

5.2. Optimal Temporal Coherence Threshold for Modelling

To ensure reliability in time series forecasting based on correlational models, it was essential to identify a minimum level of temporal coherence in the data that allows for reliable estimates. Such a threshold is determined through the analysis of the uncertainty associated with the predictions of the SBL model. Indeed, the SBL model allows estimating not only the expected output values but also the predictive variance associated with each time point, thus providing a measure of uncertainty. For this reason, for each point in the time series, uncertainty is calculated as the temporal mean of the standard deviation estimated by the SBL, subsequently normalised with respect to the maximum value observed in the dataset. In this way, each point is associated with an uncertainty index ranging between 0 and 1 (0–100%), making points with different scales comparable. The analysis focuses on the relationship between this measure of uncertainty and the temporal coherence of the data.

The main observation highlights a point of abrupt variation in uncertainty: coherence values below this threshold produce predictions with significantly higher errors, indicating that the model fails to provide reliable estimates. In other words, dataset points with low temporal coherence generate high predictive variances, making these observations of little use for monitoring or prediction. Points with coherence above the threshold, on the other hand, provide stable and quantitatively reliable predictions, outlining the set of data useful for predictive analysis. To estimate the threshold value, the set of points ordered by temporal coherence is divided into two subsets. The Root Mean Square (RMS) value of the estimated uncertainty for each subset is then calculated, and the division point that maximises the difference between the RMS of the two groups is identified, thus determining the transition point between sufficiently coherent data and incoherent data. In the analysed case study, the estimated threshold is equal to $\gamma_{th} = 0.56$, as shown in Figure 12. Under this threshold, it is possible to see that the uncertainty related to the estimates abruptly increases, making any regression model unreliable. Since the objective of the study is the prediction of ground displacements, the dataset filtered based on temporal coherence was further restricted by eliminating all points with elevation lower than -1 m or higher than 5 m. In this regard, the vertical position of PS scatterers is obtained through geocoding based on orbit timing and the reference DEM, and it may be affected by residual localisation errors and height biases (e.g., imperfect state vectors/geometry, DEM-related biases, and reference-point dependent height offsets). Therefore, to avoid discarding true basement-level scatterers that may appear slightly below the DEM-derived local ground

reference, the authors allow a small negative margin and retain PS with relative heights down to −1 m. As regards the upper elevation limit of 5 m adopted for PS selection, it is worth noting that, for the Vicoforte Sanctuary case study, the basement of the structure behaves as a rigid body. This component is a massive structural element composed of stone and brick masonry, characterised by high stiffness and limited deformability. Finite Element analyses confirm that the main vibration modes of the structure primarily involve deformation of the drum and the dome, while the basement remains substantially rigid and mechanically coupled with the underlying soil [24]. This behaviour is particularly evident below the elevation of 5 m, where the measured displacements can be reasonably attributed to soil deformation rather than to structural deformation of the building itself.

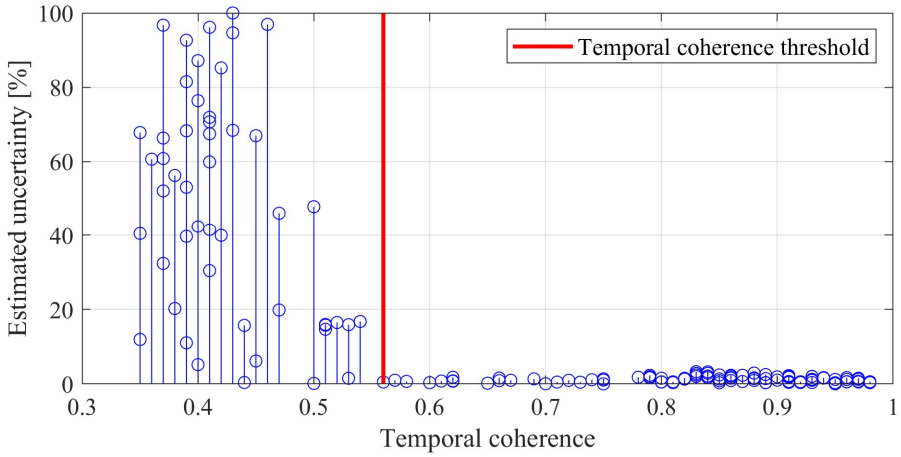


Figure 12. Estimated uncertainty function of temporal coherence. The estimated uncertainty is depicted with blue lines, the threshold temporal coherence for modelling is indicated with a red line.

5.3. Training, Validation and Testing

Starting from the points selected according to the previously defined temporal coherence threshold, a new SBL model was calibrated for predicting ground displacements. The main objective is to monitor the soil conditions, considering only coherent and representative points. For this reason, the displacement time series were preliminarily cleaned of linear trend and mean, allowing the isolation of actual variations with respect to the expected soil behaviour. This operation facilitates the assessment of deviations from the natural state and the detection of any important (e.g., pathological) changes over time.

The SBL model was trained using a constant basis function as a minimum requirement, while the order of the polynomial and trigonometric series was automatically selected through the integrated optimisation procedure. The result showed an optimal order (i.e., latent parameters) equal to 3 for the polynomial series and 1 for the trigonometric series, imposing as a constraint a minimum order of 1 for both series. The basis functions thus defined correspond to the following:

$$\mu_{*j}(x_1, x_2|\boldsymbol{c}) = w_1 + w_2x_1 + w_3x_1^2 + w_4x_1^3 + w_5sin\,(x_1) + w_6cos\,(x_1) + w_7 + w_8x_2 + w_9x_2^2 + w_{10}x_2^3 + w_{11}sin(x_2) + w_{12}cos(x_2) \quad (14)$$

where x_i represents the environmental variables considered in input (1 for surface temperature and 2 for surface humidity) and μ_{*j} the j-th predicted remote LoS displacement; w_k are the mean estimated values of the weights of the basis functions. These weights were estimated using the Relevance Vector Machine (RVM) algorithm, allowing the identification of the most significant components for displacement prediction.

As done for the first SBL model focusing on temporal coherence threshold selection, the dataset was divided in this case into training, validation, and testing. The prediction

error was evaluated using the Z-score, $Z(t)$ and normalised on the variance estimated by the model, providing a comparable measure of the reliability of the estimates. The predicted time series for each monitored point are shown in Figure 13, where it is possible to see that the model correctly fits the seasonal variation in the satellite displacements; Figure 14 represents the average error metrics, over the samples, related to training, validation, testing, and total prediction, while Table 1 reports the estimated values of the model parameters. From Figure 14, it is possible to see how the error increases from the training to the testing phase.

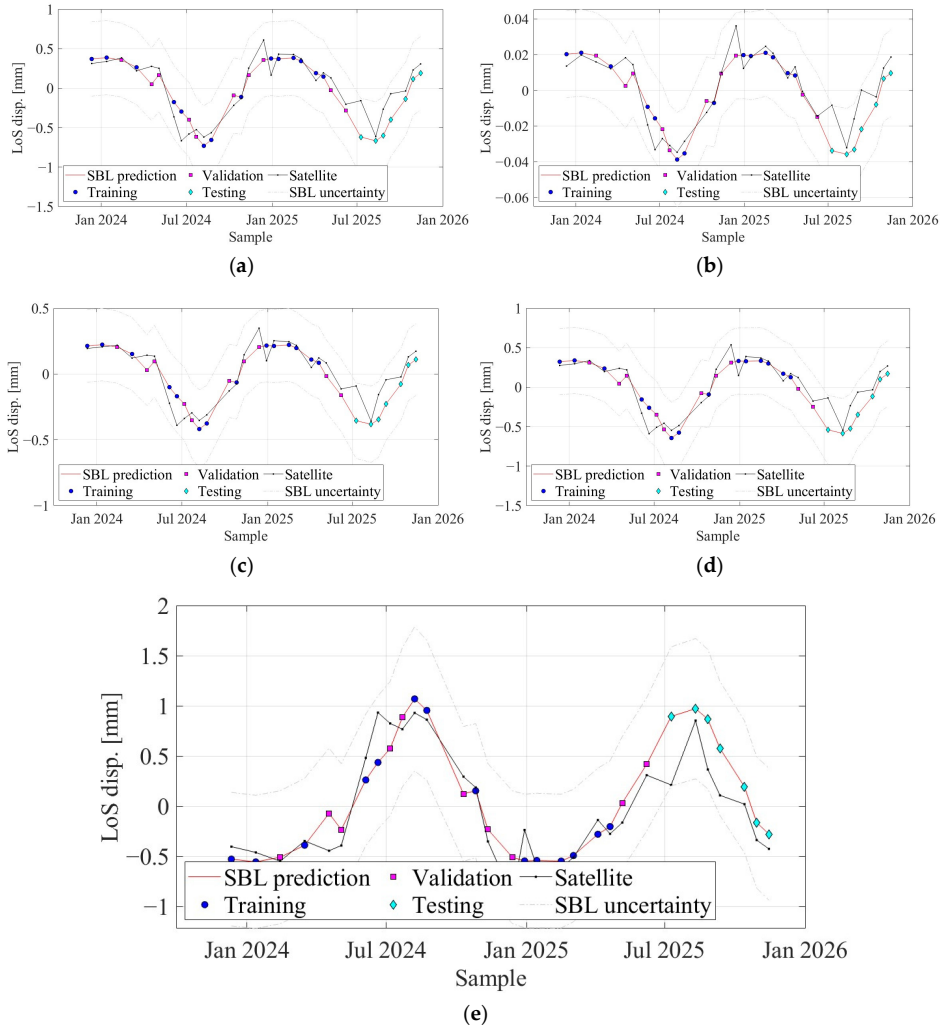


Figure 13. LoS displacement time-series predicted by the SBL optimised model for the five retained soil persistent scatterers. (**a**) point 1; (**b**) point 2; (**c**) point 3; (**d**) point 4; (**e**) point 5.

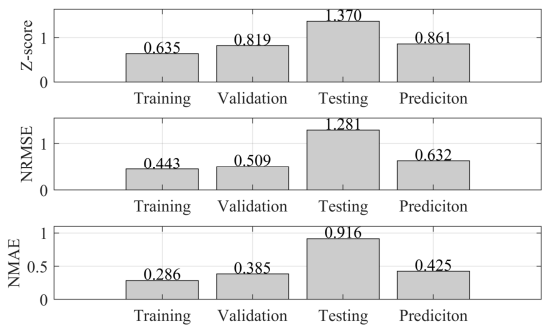


Figure 14. Average error metrics of the estimates.

In addition to the Z-score, which explicitly accounts for the uncertainty associated with the observations, complementary error metrics that do not directly incorporate uncertainty were also analysed. In particular, the Normalised Root Mean Square Error (NRMSE) and the Normalised Mean Absolute Difference (NMAD) were computed. The normalisation is done with respect to the mean absolute value of the satellite displacements. Although these metrics may lead to apparently high error values when interpreted in absolute terms, their significance must be evaluated in relation to the intrinsic uncertainty of the observations. By assuming that the measured displacement lies within a confidence interval ranging from the mean value up to the mean ± two times the standard deviation (approximately 2.5 mm for the analysed application), it is possible to define an uncertainty error threshold. Under this assumption, Z-score values lower than 2, or equivalently NRMSE or NMAD values lower than 19 (estimated as the difference between the mean displacement and the mean plus two times the standard deviation), indicate predictions that are quite lower than the observational uncertainty range and can, therefore, be considered consistent with the measurement accuracy.

Table 1. Resulting mean weight values for the five satellite displacements predicted with SBL.

μ_{*j}	w_1	w_2	w_3	w_4	w_5	w_6	w_7	w_8	w_9	w_{10}	w_{11}	w_{12}
1	2.1×10^{-1}	-3.7×10^{-9}	-1.9×10^{-3}	3.9×10^{-10}	9.1×10^{-9}	3.5×10^{-2}	2.1×10^{-1}	7.1×10^{-9}	3.4×10^{-9}	3.0×10^{-9}	-1.4×10^{-10}	5.0×10^{-9}
2	6.3×10^{-3}	-2.5×10^{-9}	-1.0×10^{-4}	-1.8×10^{-10}	8.9×10^{-9}	2.7×10^{-3}	1.6×10^{-2}	5.1×10^{-9}	1.8×10^{-9}	-9.2×10^{-11}	-6.1×10^{-9}	1.2×10^{-9}
3	1.2×10^{-1}	-7.0×10^{-9}	-1.1×10^{-3}	3.1×10^{-9}	6.7×10^{-9}	2.1×10^{-2}	1.2×10^{-1}	5.5×10^{-9}	1.5×10^{-9}	1.7×10^{-9}	1.6×10^{-9}	8.7×10^{-9}
4	1.9×10^{-1}	-4.7×10^{-9}	-1.7×10^{-3}	1.3×10^{-9}	9.3×10^{-9}	2.7×10^{-2}	1.9×10^{-1}	6.3×10^{-9}	2.6×10^{-9}	2.3×10^{-9}	5.8×10^{-10}	7.2×10^{-9}
5	-3.0×10^{-1}	-3.4×10^{-10}	2.8×10^{-3}	2.5×10^{-9}	-1.5×10^{-8}	-4.2×10^{-2}	-3.0×10^{-1}	-1.1×10^{-8}	-6.5×10^{-9}	-6.1×10^{-9}	4.3×10^{-9}	-3.5×10^{-9}

Starting from the Z-score estimated by the SBL model, a stochastic oscillator $s_o(t)$ has been introduced as a synthetic indicator for monitoring soil conditions over time. The goal is to assess how much the observed behaviour deviates, in relative terms, from what is statistically expected. The indicator was originally developed in economics and finance, where it is used to identify periods in which a variable reaches extreme values and is, therefore, likely to revert towards its mean behaviour. Transferred to the soil context, this concept is applied to the Z-score time series to identify temporal intervals in which soil displacement indicators approach their extreme bounds. Values of the stochastic oscillator close to unity define alert periods during which monitoring should be intensified to better understand the ongoing soil behaviour. If, after a prolonged monitoring phase, the oscillator exhibits a persistent divergence or a flattening of its time series, this indicates a substantial deviation of the current soil conditions from their historical behaviour. Such a response activates a second alert level, suggesting that the soil state is undergoing significant changes and that more detailed investigations may be required. The stochastic oscillator is defined as follows:

$$s_o(t) = \frac{Z(t) - Z_{min}}{Z_{max} - Z_{min}} \quad (15)$$

where t denotes time, while Z_{min} and Z_{max} respectively represent the minimum and maximum Z-score values calculated over time. In this way, the indicator takes normalised values between 0 and 1. As shown in Figure 15, the stochastic oscillator assumes values close to the threshold during periods corresponding to early July 2024 and July 2025, indicating that during the warm months, the soil behaviour tends to deviate more from what is predicted by the model. These increases are consistent with more critical thermo-hydrological conditions, which may induce variations not fully captured by the trained model with only temperature and surface humidity of the soil. Overall, however, the oscillator value remains predominantly close to 0.25, suggesting good system stability and confirming that, for most of the observation period, soil behaviour falls within expected conditions.

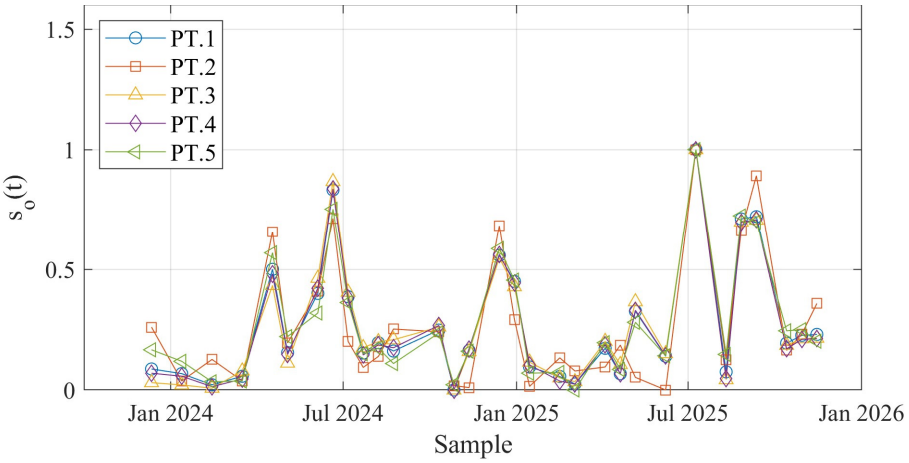


Figure 15. Stochastic oscillators for the selected points that characterise the soil close to the Sanctuary of Vicoforte.

5.4. Blind Prediction Context and Oversampling

Once the SBL model has been calibrated on the selected and validated points, it is used in a blind prediction context, relying exclusively on environmental variables as input. Specifically, the time series of surface temperature and surface soil moisture, sampled on an hourly basis, are provided to the model while keeping fixed the weights and latent parameters estimated during the training phase. In this configuration, the model does not use observed displacement information but generates predictions solely based on the learned relationships between environmental variables and soil response. This approach makes it possible to obtain hourly sampled time series of ground displacement, obtaining significant oversampling compared to the temporal resolution of satellite data, typically about 15 days. The predictions are accompanied by an uncertainty estimate, derived from the predictive variance of the SBL model, which provides a time-varying confidence interval within which the expected displacement behaviour lies.

In the analysed case study, satellite data are available until 14 November 2025. Beyond this date, the model is used to perform blind predictions of ground displacement behaviour, extending the estimate until 10 December 2025. This is possible because the input environmental variables are continuous and available almost in real-time, while satellite data have intrinsic delays that limit their immediate use for operational monitoring purposes. The blind prediction context, therefore, plays a central role in land surveillance applications. A low-cost in situ sensor capable of measuring soil temperature and moisture allows estimating, on an hourly basis, the displacement that would be observed by the satellite, anticipating its behaviour within known uncertainty thresholds. This enables a quick detection of any anomalous deviations from expected behaviour.

Figure 16 shows the time series of SBL predictions, the available satellite observations, and the associated uncertainty intervals. The figure clearly highlights the continuity of prediction beyond the last satellite observation and the stability of confidence intervals during the blind prediction period. Once satellite data become available, they can be immediately compared with the prediction, allowing for posterior validation and identification of anomalous soil behaviours.

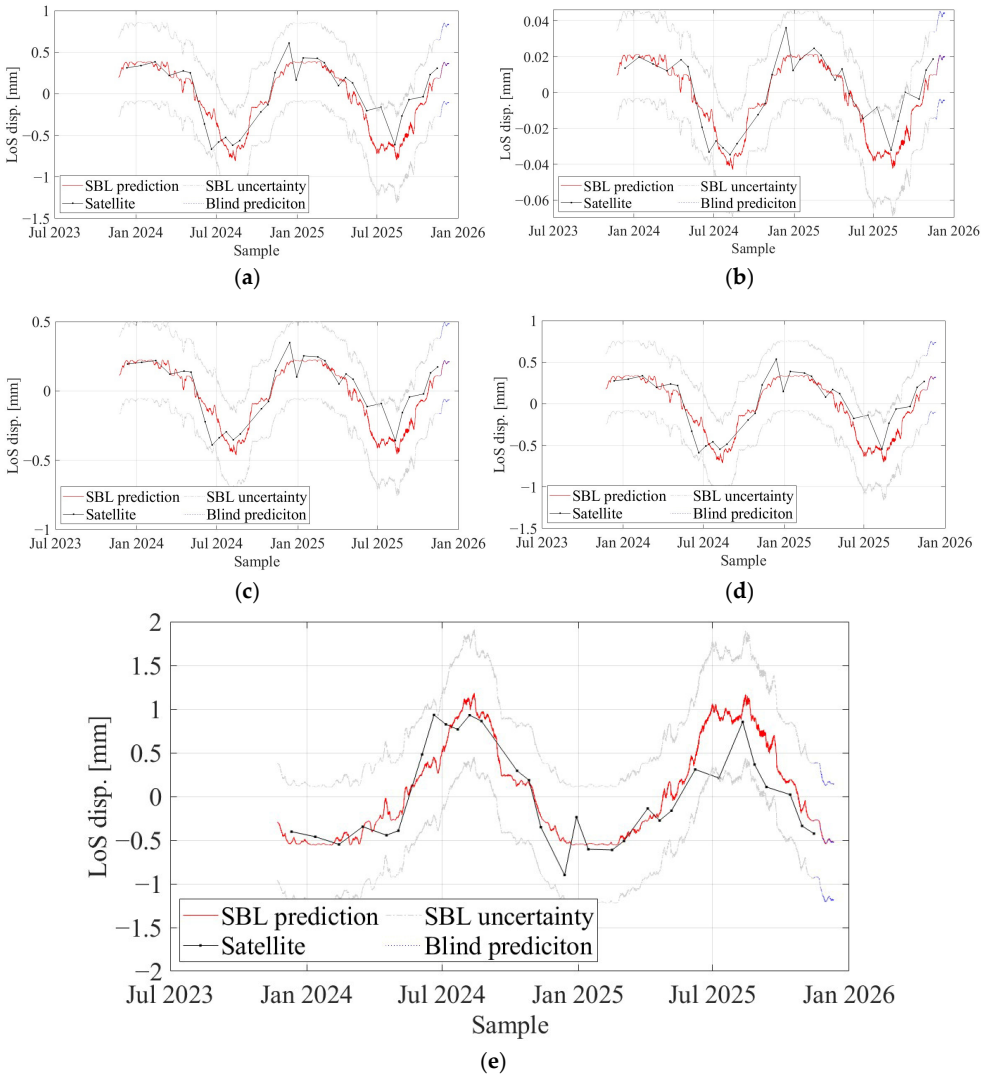


Figure 16. Oversampled LoS displacement time-series predicted by the SBL optimised model for the five retained soil persistent scatterers. The prediction was based on the original sampling time of the input quantities, i.e., 1 h. (**a**) point 1; (**b**) point 2; (**c**) point 3; (**d**) point 4; (**e**) point 5.

6. Conclusions

This work proposes a coherent methodological framework for integrating PS-InSAR data and low-cost environmental sensors, explicitly addressing the role of temporal coherence in data-driven modelling of ground displacements. In more detail, the analysis highlighted that the temporal coherence of PS is not only a quality indicator of the time-series, but it also introduces a physical and spatial bias that significantly affects inferences on ground deformation phenomena. The conclusions of the study are reported hereinafter:

- The analysis of predictive uncertainty provided by SBL allows for the identification of a temporal coherence threshold beyond which PS time series are reliable for modelling. In the analysed case study, an optimal coherence threshold of about 0.56 was identified, below which uncertainty increases to an unacceptable level.

- The integration of selected PS-InSAR data with soil temperature and surface moisture enables a robust reproduction of the seasonal and non-linear components of the displacements observed along the satellite line of sight.
- For the case study, the stochastic oscillator showed predominant values at approximately 0.25 with peaks close to 1 during the warm months, highlighting the overall stability of the soil in the analysed period.
- The calibrated SBL model allowed for a temporally denser reconstruction of displacements compared to the satellite revisit frequency, while maintaining a quantitative estimate of uncertainty.
- The approach demonstrates that low-cost in situ sensors can effectively support continuous monitoring of soil behaviour, reducing reliance on more expensive direct measurements.

Future developments will include the extension to multi-constellation and multi-geometry data for three-dimensional reconstruction of displacements, the inclusion of non-linear soil response models in the SBL framework, and the application of the framework to contexts with faster and more complex soil dynamics, in order to assess its operational generalizability.

Author Contributions: R.T.: Conceptualisation, Data curation, Formal analysis, Investigation, Methodology, Resources, Validation, Visualisation, Writing—original draft, Writing—review and editing. G.M.: Conceptualisation, Data curation, Investigation, Methodology, Resources, Supervision, Validation, Visualisation, Writing—review and editing. S.C.: Conceptualisation, Data curation, Investigation, Methodology, Resources, Supervision, Validation, Visualisation, Writing—review and editing. R.C.: Project administration, Supervision, Writing—review and editing. G.A.F.: Supervision, Writing—review and editing. All authors have read and agreed to the published version of the manuscript.

Funding: This research received no external funding.

Data Availability Statement: The rights of the in situ data used are owned by the Amministrazione del Santuario di Vicoforte and cannot be shared.

Acknowledgments: This research was carried out within the DPC/ReLUIS 2024–2026 project—WP6 Monitoraggio e Dati Satellitari (in Italian).

Conflicts of Interest: The authors declare no conflicts of interest.

References

1. Ferretti, A.; Prati, C.; Rocca, F. Permanent Scatterers in SAR Interferometry. *IEEE Trans. Geosci. Remote Sens.* **2001**, *39*, 8–20. [CrossRef]
2. Hooper, A.; Zebker, H.; Segall, P.; Kampes, B. A New Method for Measuring Deformation on Volcanoes and Other Natural Terrains Using InSAR Persistent Scatterers. *Geophys. Res. Lett.* **2004**, *31*, L23611. [CrossRef]
3. Crosetto, M.; Monserrat, O.; Ferro, A.; Serra, M. Persistent Scatterer Interferometry: A Review. *ISPRS J. Photogramm. Remote Sens.* **2016**, *115*, 78–89. [CrossRef]
4. Antonielli, B.; Sciortino, A.; Scancella, S.; Bozzano, F.; Mazzanti, P.; Antonielli, B.; Sciortino, A.; Scancella, S.; Bozzano, F.; Mazzanti, P. Tracking Deformation Processes at the Legnica Glogow Copper District (Poland) by Satellite InSAR—I: Room and Pillar Mine District. *Land* **2021**, *10*, 653. [CrossRef]
5. Mazzanti, P.; Antonielli, B.; Sciortino, A.; Scancella, S.; Bozzano, F. Tracking Deformation Processes at the Legnica Glogow Copper District (Poland) by Satellite InSAR—Part II: Żelazny Most Tailings Dam. *Land* **2021**, *10*, 654. [CrossRef]
6. Moretto, S.; Bozzano, F.; Mazzanti, P. The Role of Satellite InSAR for Landslide Forecasting: Limitations and Openings. *Remote Sens.* **2021**, *13*, 3735. [CrossRef]
7. Ghaderpour, E.; Mazzanti, P.; Bozzano, F.; Scarascia Mugnozza, G. Ground Deformation Monitoring via PS-InSAR Time Series: An Industrial Zone in Sacco River Valley, Central Italy. *Remote Sens. Appl. Soc. Environ.* **2024**, *34*, 101191. [CrossRef]
8. Kalavrezou, I.E.; Loupasakis, C.; Patsioti, E.; Sakkas, V.; Pavlides, S. Application of Time Series InSAR (SBAS) Method Using Sentinel-1 Data for Coupling Ground Deformation and Seismic Activity in Greece. *Land* **2024**, *13*, 485. [CrossRef]

9. Ceravolo, R.; De Marinis, A.; Pecorelli, M.L.; Zanotti Fragonara, L. Monitoring of Masonry Historical Constructions: 10 Years of Static Monitoring of the World's Largest Oval Dome. *Struct. Control Health Monit.* **2017**, *24*, e1988. [CrossRef]
10. Pecorelli, M.; Ceravolo, R.; Epicoco, R. An Automatic Modal Identification Procedure for the Permanent Dynamic Monitoring of the Sanctuary of Vicoforte. *Int. J. Archit. Herit.* **2020**, *14*, 630–644. [CrossRef]
11. Coccimiglio, S.; Coletta, G.; Lenticchia, E.; Miraglia, G.; Ceravolo, R. Combining Satellite Geophysical Data with Continuous On-Site Measurements for Monitoring the Dynamic Parameters of Civil Structures. *Sci. Rep.* **2022**, *12*, 2275. [CrossRef]
12. Coccimiglio, S.; Coletta, G.; Ceravolo, R. Use of Copernicus Satellite Data to Investigate the Soil-Structure Interaction and Its Contribution to the Dynamics of a Monitored Monumental Building. In Proceedings of the 1st Conference of the European Association on Quality Control of Bridges and Structures (EUROSTRUCT 2021), Padua, Italy, 29 August–1 September 2021; Springer: Cham, Switzerland, 2022; pp. 1171–1179. [CrossRef]
13. Sousa, J.J.; Ruiz, A.M.; Hanssen, R.F.; Bastos, L.; Gil, A.J.; Galindo-Zaldívar, J.; Sanz De Galdeano, C. PS-InSAR Processing Methodologies in the Detection of Field Surface Deformation—Study of the Granada Basin (Central Betic Cordilleras, Southern Spain). *J. Geodyn.* **2010**, *49*, 181–189. [CrossRef]
14. Kizilirmak, G.; Cakir, Z. Application of PS-InSAR and Diagnostic Train Measurement Techniques for Monitoring Subsidence in High-Speed Railway in Konya, Türkiye. *Infrastructures* **2024**, *9*, 152. [CrossRef]
15. Maghsoudi, Y.; Van Der Meer, F.; Hecker, C.; Perissin, D.; Saepuloh, A. Using PS-InSAR to Detect Surface Deformation in Geothermal Areas of West Java in Indonesia. *Int. J. Appl. Earth Obs. Geoinf.* **2018**, *64*, 386–396. [CrossRef]
16. Jiang, Y.; Yu, X. Space-Based Long Term Condition Monitoring of Cold Region Pavement with PS-InSAR. *J. Infrastruct. Preserv. Resil.* **2025**, *6*, 4. [CrossRef]
17. Zhou, Y.; Hao, G.; Chen, J.; Wei, J. Time Series Forecasting and Anomaly Detection of Bridge Deformation Based on PS-InSAR Technique and Seasonal-Trend Decomposition. *Struct. Health Monit.* **2025**, 14759217251365289. [CrossRef]
18. Ferretti, A.; Prati, C.; Rocca, F. Nonlinear Subsidence Rate Estimation Using Permanent Scatterers in Differential SAR Interferometry. *IEEE Trans. Geosci. Remote Sens.* **2000**, *38*, 2202–2212. [CrossRef]
19. Berardino, P.; Fornaro, G.; Lanari, R.; Sansosti, E. A New Algorithm for Surface Deformation Monitoring Based on Small Baseline Differential SAR Interferograms. *IEEE Trans. Geosci. Remote Sens.* **2002**, *40*, 2375–2383. [CrossRef]
20. Perissin, D.; Rocca, F. High Accuracy Urban DEM Using Permanent Scatterers. *IEEE Trans. Geosci. Remote Sens.* **2006**, *44*, 3338–3347. [CrossRef]
21. Perissin, D.; Wang, T. Repeat-Pass SAR Interferometry with Partially Coherent Targets. *IEEE Trans. Geosci. Remote Sens.* **2012**, *50*, 271–280. [CrossRef]
22. Perissin, D. SarProZ© 2025. Available online: https://www.sarproz.com (accessed on 4 February 2026).
23. Perissin, D.; Wang, Z.; Wang, T. The SARPROZ InSAR Tool for Urban Subsidence/Manmade Structure Stability Monitoring in China. In Proceedings of the 34th International Symposium on Remote Sensing of Environment (ISRSE 2011), Sydney, Australia, 10–15 April 2011.
24. Ceravolo, R.; De Lucia, G.; Miraglia, G.; Pecorelli, M.L. Thermoelastic Finite Element Model Updating with Application to Monumental Buildings. *Comput.-Aided Civ. Infrastruct. Eng.* **2020**, *35*, 628–642. [CrossRef]
25. Nakamura, Y. A Method for Dynamic Characteristics Estimation of Subsurface Using Microtremor on the Ground Surface. *Q. Rep. Railw. Tech. Res. Inst.* **1989**, *30*, 25–33.
26. SESAME European Research Project. *Guidelines for the Implementation of the H/V Spectral Ratio Technique on Ambient Vibrations: Measurements, Processing and Interpretation*; European Commission, Research Directorate-General: Brussels, Belgium, 2004. Available online: https://sesame.geopsy.org/Delivrables/Del-D23-HV_User_Guidelines.pdf (accessed on 4 February 2026).
27. Molnar, S. A Review of the Microtremor Horizontal-to-Vertical Spectral Ratio (HVSR) Method. *J. Seismol.* **2022**, *26*, 653–685. [CrossRef]
28. Neukirch, A. Horizontal-to-Vertical Spectral Ratio of Ambient Vibration for Site Characterization: A Review. *Sensors* **2021**, *21*, 3292. [CrossRef]
29. Tipping, M.E. Sparse Bayesian Learning and the Relevance Vector Machine. *J. Mach. Learn. Res.* **2001**, *1*, 211–244. [CrossRef]
30. Huang, Y.; Beck, J.L. Hierarchical Sparse Bayesian Learning for Structural Health Monitoring with Incomplete Modal Data. *Int. J. Uncertain. Quantif.* **2015**, *5*, 139–169. [CrossRef]
31. Agram, P.S.; Simons, M. A Noise Model for InSAR Time Series. *J. Geophys. Res. Solid Earth* **2015**, *120*, 2752–2771. [CrossRef]
32. Lai, C.G.; Corigliano, M.; Sanchez, H.; Scandella, L. *Definition of Seismic Input at the Regina Montis Regalis Basilica of Vicoforte, Northern Italy*; IUSS Press: Pavia, Italy, 2009.

Disclaimer/Publisher's Note: The statements, opinions and data contained in all publications are solely those of the individual author(s) and contributor(s) and not of MDPI and/or the editor(s). MDPI and/or the editor(s) disclaim responsibility for any injury to people or property resulting from any ideas, methods, instructions or products referred to in the content.